


Oxygen Evolution Reaction **Hot Paper**


Boosting Photocatalytic Water Oxidation Over Bifunctional Rh^0 - Rh^{3+} Sites

 Yuanwei Liu⁺, Li Jie Wang⁺, Hao Zhang, Hai Yang Yuan, Qinghua Zhang, Lin Gu, Hai Feng Wang, P. Hu, Peng Fei Liu,^{*} Zheng Jiang,^{*} and Hua Gui Yang^{*}

Abstract: Photocatalytic water splitting provides an economically feasible way for converting solar energy into hydrogen. Great efforts have been devoted to developing efficient photocatalysts; however, the surface catalytic reactions, especially for the sluggish oxygen evolution reaction (OER), still remain a challenge, which limits the overall photocatalytic energy efficiency. Herein, we design a Rh_n cluster cocatalyst, with Rh^0 - Rh^{3+} sites anchoring the Mo-doped $BiVO_4$ model photocatalytic system. The resultant photocatalyst enables a high visible-light photocatalytic oxygen production activity of $7.11 \text{ mmol g}^{-1} \text{ h}^{-1}$ and an apparent quantum efficiency of 29.37% at 420 nm. The turnover frequency (TOF) achieves 416.73 h^{-1} , which is 378 times higher than that of the photocatalyst only with Rh^{3+} species. Operando X-ray absorption characterization shows the OER process on the Rh^0 - Rh^{3+} sites. The DFT calculations further illustrate a bifunctional OER mechanism over the Rh^0 - Rh^{3+} sites, in which the oxygen intermediate attacks the Rh^{3+} sites with assistance of a hydrogen atom transfer to the Rh^0 sites, thus breaking the scaling relationship of various oxygen intermediates.

Introduction

Solar-driven hydrogen production is generally regarded as a promising strategy to address the environmental crises and energy shortage issues.^[1] Particularly, the photocatalytic water splitting via using semiconductor photocatalysts provides a clean, convenient and sustainable approach for hydrogen production. In general, there are three main steps in photocatalytic water splitting: the generation of electron-hole pairs by absorbing solar light, the separation and migration of the

How to cite: *Angew. Chem. Int. Ed.* **2021**, *60*, 22761–22768
 International Edition: doi.org/10.1002/anie.202106874
 German Edition: doi.org/10.1002/ange.202106874

charge carriers, and H_2 and O_2 evolution reactions at the surface of catalysts. To improve the efficiency of photocatalytic water splitting, numerous efforts have been put for the first two steps in the last few decades;^[2] unfortunately, its overall energy efficiency is still limited by the sluggish surface catalytic reactions in the third step which could be promoted by cocatalysts.^[3] Since the pioneering works by Bard et al. in 1978 reporting the photodeposition of Pt onto TiO_2 for potential photocatalytic applications,^[4] variety of cocatalysts (e.g., noble metal, metal sulfides, metal phosphides, metal-free and MXene materials) have demonstrated their effectiveness when combined with proper semiconductor-based host photocatalysts.^[3a,5] Besides the discovery of new efficient cocatalysts, the local structural modification of the cocatalysts can also optimize their catalytic activities. Our previous works have confirmed the contribution of the positively-charged Pt-based cocatalysts for the boosted photocatalytic hydrogen evolution reaction (HER).^[6] However, modifying local structures of cocatalysts is still an open challenge to further enhance the overall photocatalytic efficiency.

The oxygen evolution reaction (OER) commonly involves a four consecutive proton-coupled electron transfer (PCET) in the water splitting process.^[7] Unlike the HER process which undergoes only hydrogen intermediate, the OER process typically features various oxygen intermediates, suffering from scaling relationship in adsorption energies of $*OH$, $*O$ and $*OOH$ intermediates.^[7,8] This induces serious challenges to break the scaling relationship to obtain efficient OER catalysts. Until now, single-site modification has been widely used to maximize the unitization of active sites with simultaneously optimized absorption energy of intermedi-

[*] Y. Liu,^[†] L. J. Wang,^[†] Dr. H. Y. Yuan, Dr. P. F. Liu, Prof. H. G. Yang
 Key Laboratory for Ultrafine Materials of Ministry of Education,
 School of Materials Science and Engineering, East China University
 of Science and Technology
 130 Meilong Road, Shanghai 200237 (China)
 E-mail: pflu@ecust.edu.cn
 hgyang@ecust.edu.cn

Y. Liu,^[†] Dr. H. Zhang, Prof. Z. Jiang
 Shanghai Synchrotron Radiation Facility, Shanghai Institute of
 Applied Physics, Chinese Academy of Sciences
 Shanghai 201204 (China)
 E-mail: jiangzheng@sinap.ac.cn

Dr. Q. Zhang, Prof. L. Gu
 Laboratory for Advanced Materials and Electron Microscopy, Insti-
 tute of Physics, Chinese Academy of Sciences
 Beijing 100190 (China)

Prof. H. F. Wang
 Key Laboratory for Advanced Materials, School of Chemistry and
 Molecular Engineering, East China University of Science and
 Technology
 130 Meilong Road, Shanghai 200237 (China)

Prof. P. Hu
 School of Chemistry and Chemical Engineering, The Queen's
 University of Belfast
 Belfast BT9 5AG (UK)

Prof. Z. Jiang
 Shanghai Synchrotron Radiation Facility, Shanghai Advanced Re-
 search Institute, Chinese Academy of Sciences
 Shanghai 201204 (China)

[†] These authors contributed equally to this work.

 Supporting information and the ORCID identification number(s) for
 the author(s) of this article can be found under:
 <https://doi.org/10.1002/anie.202106874>.

ates,^[9] but this strategy is still limited in the optimization of catalytic activity involving multiple intermediates. Very recently, the bifunctional OER mechanism over two different metal catalytic sites has been proposed to break the OER scaling relationship in the electrocatalytic OER process, with one catalytic site serving as electrophilic site to adsorb hydroxide assisted by the concerted hydrogen transfer to the neighbouring catalytic site, which could synergistically lower the OER energies.^[10] Inspired by this, we anticipate a highly active OER cocatalyst can be constructed via elaborate incorporation of bifunctional sites featuring the potential to break the OER scaling relationship.

Herein, we rationally constructed an OER cocatalyst of bifunctional Rh_n cluster, consisting of atomically dispersed oxidized Rh³⁺ sites adjacent to metallic Rh⁰ sites. The resultant bifunctional Rh_n cocatalyst anchored on Mo-doped BiVO₄ which is widely used as the classic and stable light-absorber material in the particulate photocatalytic sheets or photoanodes,^[11] achieves an excellent photocatalytic OER performance of 7.11 mmol g⁻¹ h⁻¹. We believe the concept of bifunctional Rh⁰-Rh³⁺ sites can provide new opportunities for atomic-scale control of cocatalyst to construct OER-related solar energy related techniques.

Results and Discussion

Crystal and electronic structural analysis

The host photocatalyst of Mo-doped BiVO₄ (named as BVOM) was obtained from Mo-doped K₃V₅O₁₄ and Bi(NO₃)₃·5H₂O with a simple stirring method.^[11b,12] Rh-based cocatalysts incorporation was implemented through a subtle pH-control impregnation method which can synthesize ultra-small clusters,^[13] to give trace-amount Rh-loaded BVOM (RBVOM) precursor. Furthermore, the diverse valence states of Rh was precisely modulated via calcination treatments at the different atmosphere of air or hydrogen to obtain RBVOM-A (decorated with only Rh³⁺ sites) or RBVOM-H (decorated with Rh⁰-Rh³⁺ sites) samples, respectively (Figure 1a, more preparation details were described in the supporting information).

Scanning electron microscopy (SEM) and transmission electron microscopy (TEM) were firstly conducted to study the morphology of pristine BVOM sample. In Figure S1 and 1b, the SEM and TEM images of the BVOM sample exhibit the decahedral morphology, which indicates that BVOM can be used as an ideal model host photocatalyst.^[11a,14] Figure 1c and Figure S2 exhibit the typical high angle annular dark-field scanning transmission electron microscopy (HAADF-STEM) images, in which the lattice fringes of 0.457, 0.305 and 0.310 nm could be observed, which are indexed to (101), (013) and (-112) planes of the monoclinic scheelite BiVO₄ (according to JCPDS standard card #97-010-0605). This is consistent with the fast Fourier transformation (FFT) image of BiVO₄ along the [13-1] zone axis in Figure 1d. Furthermore, the inverse FFT (IFFT) image of the selected area in Figure 1d matches well with corresponding simulated atomic distribution, indicating an ordered atomic arrangement in

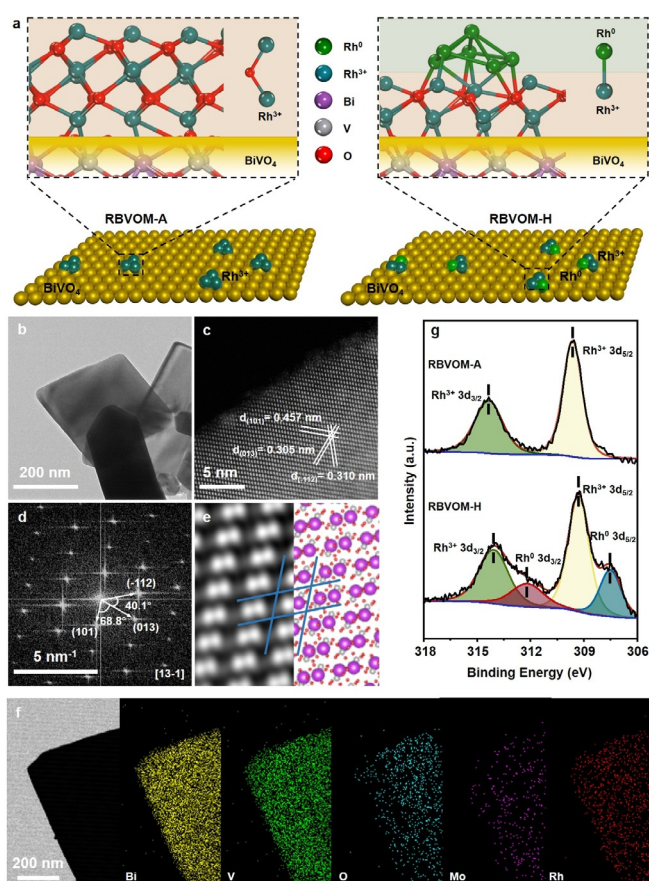


Figure 1. Schematic illustration and corresponding characterization of crystal and electronic structures. a) Abridged general view of RBVOM-A (only decorated with Rh³⁺ sites) and RBVOM-H (decorated with Rh⁰-Rh³⁺ sites) with corresponding atomic structures. b) TEM image of the BVOM, showing the decahedral morphology. c) The atomic-resolution HAADF-STEM image of the BVOM and d) FFT pattern along the [13-1] zone axis of BVOM in (c), indicating the monoclinic BiVO₄ structure. e) IFFT of the selected area in (d) (left) and the corresponding simulated unit cell of BiVO₄ (right), with purple Bi, red O, gray V. f) TEM image of RBVOM-H and the corresponding EDX mapping images of Bi, V, O, Mo and Rh elements, respectively, illustrating the uniform distribution of the loaded Rh_n cocatalyst. g) XPS spectra of RBVOM-A and RBVOM-H samples in the Rh 3d region, showing differentiable Rh³⁺ and Rh⁰ species in RBVOM-H.

BVOM (Figure 1e). The crystal structural analysis of BVOM demonstrates the well-crystalline feature of the host photocatalyst, which can provide the explicit platform to study the effects of cocatalysts.

After Rh incorporation, the crystal structures of BVOM, RBVOM-A and RBVOM-H were studied via X-ray diffraction (XRD) analysis (Figure S3), exhibiting that BVOM is well-indexed to monoclinic scheelite BiVO₄. The diffraction peaks of Rh-loaded BVOM present no obvious changes and no obvious Rh clusters or particles could be observed in the bright field STEM (BF-STEM) and HAADF-STEM images (Figure S4), suggesting the ultrasmall particle size and low-weight loading of Rh species on surface of BVOM.^[15] In addition, the SEM and TEM of RBVOM-H were also conducted (Figure S5), which indicates the negligible mor-

phology changes compared with the pristine BVOM. The energy dispersive X-ray mapping (EDX, Figure 1 f) images of RBVOM-H show the homogeneously dispersed elements, proving that the Rh_n cocatalysts are uniformly anchored on the BVOM. Inductively coupled plasma-optical emission spectroscopy (ICP-OES, Table S1) was also implemented to detect the cocatalyst loading, which also demonstrates the ultralow amount of Rh cocatalyst (0.28 wt.%) and Mo dopants (0.01 wt.%).

To analyze the surface electronic structure, X-ray photoelectron spectroscopy (XPS) characterizations of BVOM, RBVOM-A and RBVOM-H were conducted. As shown in Figure S6, there is no obvious difference in the Bi 4f and V 2p XPS spectra of BVOM, RBVOM-H and RBVOM-A, indicating that Rh incorporation and thermal treatment would not obviously affect the surface electronic structures of the bulk host photocatalyst. However, the XPS spectra in the Rh 3d region of RBVOM-A and RBVOM-H obtained at different atmosphere exhibit sharp differences (Figure 1 g). Compared with RBVOM-A, obvious new peaks at 307.5 and 312.1 eV in the Rh $3d_{5/2}$ and Rh $3d_{3/2}$ regions were observed for RBVOM-H, which are assigned to the metallic state of Rh^0 species.^[16] Furthermore, H_2 temperature-programmed reduction (H_2 -TPR) was conducted to prove whether or not the surface elements of BVOM could be reduced by hydrogen treatment. In Figure S7, there is a hydrogen consumption peak at 130 °C in the spectrum of RBVOM, while no peaks appear in that of BVOM within 50–300 °C, demonstrating that hydrogen treatment did reduce oxidized Rh species instead of the surface elements of the pristine BVOM.^[17] Based on the above characterizations, we demonstrate that the obtained samples have well-defined morphology and good crystallinity, and the main difference between RBVOM-A and RBVOM-H is the valence states between the Rh cocatalysts: only Rh^{3+} species exist in RBVOM-A, while RBVOM-H features the coexistence of characteristic Rh^0 and Rh^{3+} .

Local structure investigation of anchored Rh species

To further identify the true states of Rh species in RBVOM-H and RBVOM-A, X-ray absorption fine structure (XAFS) characterizations were conducted. Firstly, V K-edge and Bi L_{3-} -edge XAFS were conducted, as shown in Figure S8, the spectra of normalized X-ray absorption near-edge structure (XANES), extended X-ray absorption fine structure

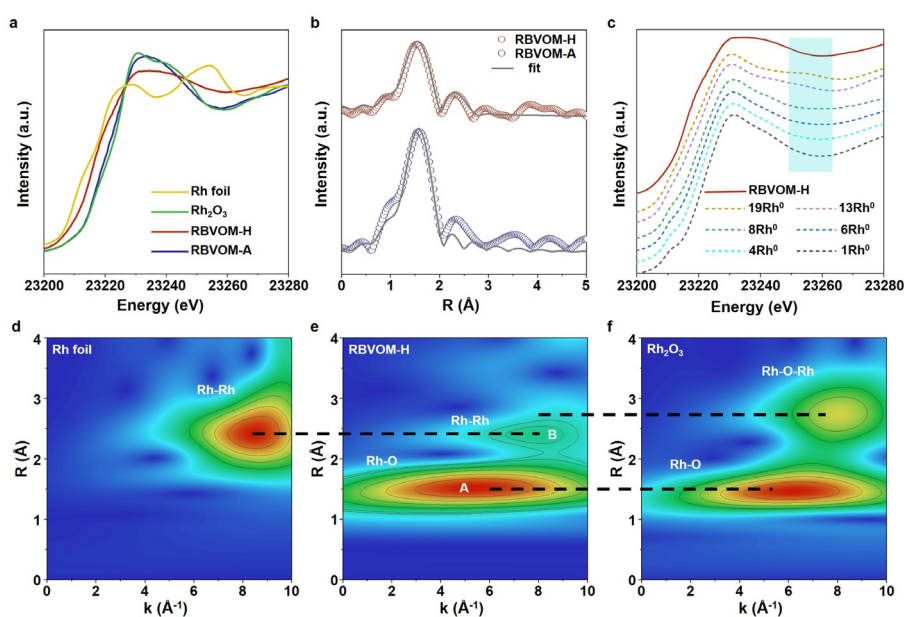


Figure 2. Local structure characterizations of RBVOM-H and controls. a) Rh K-edge XANES and b) corresponding EXAFS spectra along with fits of RBVOM-H and RBVOM-A samples, indicating the coexistence of oxidized Rh^{3+} and metallic Rh^0 in the RBVOM-H. c) The experimental XANES spectra of RBVOM-H and the corresponding calculations of XANES spectra configured with different atom numbers of metallic Rh^0 on the oxidized Rh_2O_3 , showing the characteristic configuration of a small number of metallic Rh^0 atoms adjacent Rh^{3+} species. The numbers in front of Rh^0 represent the atom numbers of Rh^0 in the configuration. d)–f) WT contour plots of k^2 -weighted $\chi(k)$ signals from Rh foil, RBVOM-H and Rh_2O_3 , confirming the peculiar oxidized Rh–O and metallic Rh–Rh bonds in RBVOM-H. The absence of Rh–O–Rh also suggests that no aggregated Rh^{3+} species (Rh_2O_3 particles or clusters) in RBVOM-H.

(EXAFS) and Fourier-transformed EXAFS (FT-EXAFS) of V K-edge and Bi L_{3-} -edge show no obvious differences, which suggests the bulk structures of $BiVO_4$ are not responsible for performance discrepancy of RBVOM-H and RBVOM-A. Figure 2a shows the Rh K-edge normalized XANES, and the spectrum of RBVOM-A is in the same position with Rh_2O_3 ; for comparison, the position of RBVOM-H is between Rh foil and Rh_2O_3 , illustrating that the bulk valence state of Rh in RBVOM-A is Rh^{3+} and in RBVOM-H that is the mixture of Rh^0 and Rh^{3+} , which is consistent with XPS results. The Fourier-transformed spectra of the Rh K-edge EXAFS and corresponding fits for RBVOM-H and RBVOM-A are displayed in Figure 2b, combining the fitting parameters listed in Table S2, with only Rh–O (2.03 Å) and Rh–Cl (2.25 Å) exist in RBVOM-A while Rh–O (2.04 Å) and Rh–Rh (2.67 Å) coordination exist in RBVOM-H. It is mentionable that no Rh–O–Rh (typically 3.02 Å in Rh_2O_3) coordination could be fitted in RBVOM-A or RBVOM-H, indicating the small size of Rh-based cocatalysts in RBVOM-A and RBVOM-H. Thus, the structure differences of Rh species between RBVOM-A and RBVOM-H are identified: there are only Rh^{3+} species in RBVOM-A, while Rh^0 and Rh^{3+} species coexisted in the Rh_n cocatalyst of RBVOM-H to form Rh^0 - Rh^{3+} sites.

To further determine the configurations of Rh^0 - Rh^{3+} sites in RBVOM-H, theoretical calculation of XANES with the FDMNES code^[18] and wavelet transform (WT) of k^2 -weighted $\chi(k)$ signals based on Morlet wavelets^[19] were carried out.

In Figure 2c, the full-line curve representing RBVOM-H is an experimental spectrum, while the other dashed-line curves represent the calculated different atom numbers of metallic Rh⁰, which is adjacent the oxidized Rh³⁺ species (Figure S9). It can be seen that with the increase of metallic Rh⁰ atom numbers, the peak valley around 23260 eV heightens until an obvious new peak appears, and the most similar curves are that consists of 6 and 8 metallic Rh⁰ atoms on Rh₂O₃, indicating that Rh⁰ species in RBVOM-H consist of a small number of Rh⁰ atoms. Figure 2d–f and Figure S10 show the Morlet wavelet transform (WT) contour plots, and the location of intensity maximum is mainly related to the bond length R (R direction) and atomic number Z (k direction). The intensity maximum A and B correspond to oxidized Rh–O coordination of Rh₂O₃ and metallic Rh–Rh coordination of Rh foil both on k and R directions, which verifies the coexistence of Rh–O (oxidized Rh³⁺ species) and Rh–Rh (metallic Rh⁰ species) in RBVOM-H. The WT contour plots of RBVOM-A was also analyzed (Figure S11), which shows the only intensity maximum is assigned to Rh–O(Cl) coordination. Consistent with the fitting results, no Rh–O–Rh bonds were observed in RBVOM-H and RBVOM-A, suggesting that no aggregated Rh³⁺ species (e.g., Rh₂O₃ particles) could be found. These results unambiguously demonstrate the atomically dispersed Rh³⁺ species adjacent to Rh⁰ clusters, which could promote the electron-hole separation and maximize the utilization of Rh⁰–Rh³⁺ sites.

Photocatalytic OER performance evaluation

To gain an insightful understanding of the bifunctional Rh⁰–Rh³⁺ sites in the photocatalytic processes of RBVOM-H, various characterizations on its photoelectrochemical properties were performed. Ultraviolet-visible diffuse reflectance spectroscopy (UV-Vis DRS, Figure S12) analysis shows that all the obtained samples exhibit similar absorption edges, indicating that the Rh-based cocatalysts loading with different valence states has negligible effects on the light absorption ability of BVOM. The steady-state photoluminescence (PL) spectra indicate that the charge recombination would be effectively suppressed after cocatalysts loading (Figure S13). The transient photocurrent responses demonstrate the highest photocurrent density for RBVOM-H (Figure S14). We further collected the samples for electrochemical impedance spectroscopy (EIS) test (Figure S15), and the EIS spectra also illustrate the RBVOM-H has smaller charge transfer resistance and faster interfacial electron transfer than other photocatalysts.

The photocatalytic OER performance of BVOM, RBVOM-A and RBVOM-H were evaluated under visible light irradiation (Figure 3a,b and Figure S16). The pristine pure BVOM without cocatalyst loading exhibits a low photocatalytic oxygen production rate of $2.28 \pm 0.12 \text{ mmol g}^{-1} \text{ h}^{-1}$. After Rh loading, the oxygen production rate shows clear differences. For hydrogen-treated Rh-based cocatalyst decorated RBVOM-H, the oxygen production rate is up to $7.11 \pm 0.05 \text{ mmol g}^{-1} \text{ h}^{-1}$ with the optimized loading amount of theoretical 0.6 wt.% Rh (Figure S17). However, for the

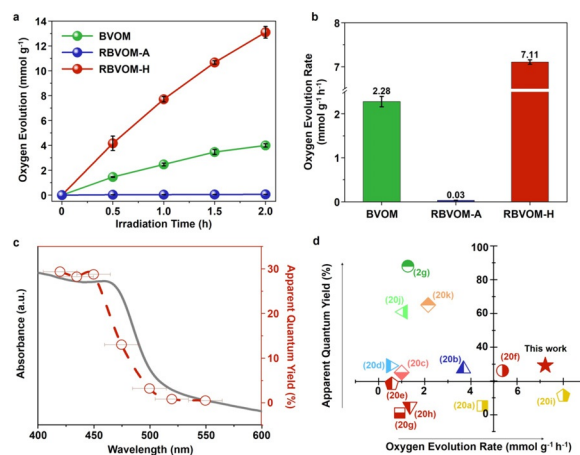


Figure 3. Photocatalytic OER performance of RBVOM-H and controls. a) Time-dependent photocatalytic oxygen production amounts in the presence of silver nitrate (0.05 M) as a sacrificial agent under visible light irradiation ($\lambda > 420 \text{ nm}$) and b) photocatalytic OER rates of BVOM, RBVOM-A and RBVOM-H, showing the optimal performance up to $7.11 \pm 0.05 \text{ mmol g}^{-1} \text{ h}^{-1}$ for RBVOM-H. Error bars in (a) and (b) were counted from 3 individual samples. Calculation methods of oxygen evolution rate: the data were taken from 0 to 1.5 hours of oxygen production to amount for linear fitting, and the slope k is the oxygen evolution rate. c) UV-vis and AQY of RBVOM-H, which were plotted at the center wavelengths of the band-pass filters, with error bars showing the deviation of the wavelengths ($\Delta\lambda = 15 \text{ nm}$). d) oxygen production rate and AQY for RBVOM-H and representative water oxidation photocatalysts. The corresponding reference numbers were included in brackets,^[2g,20] and more details were shown in Table S3.

Rh³⁺ species dominant cocatalysts, RBVOM-A shows a deteriorated activity of $0.03 \pm 0.01 \text{ mmol g}^{-1} \text{ h}^{-1}$. From the Fourier-transformed spectra of the Rh K-edge EXAFS fitting results for RBVOM-H and RBVOM-A (Table S2), it can be seen that Rh–Cl coordination only exists in RBVOM-A rather than RBVOM-H. Based on the results, phase diagrams of RhCl₃ and Rh₂O₃ to Rh were calculated (Figure S18), which indicates that Cl[−] might be easily removed in the synthesis of RBVOM-H, and suggests the crucial role of Rh–Cl coordination on the generation of Rh⁰ to form Rh⁰–Rh³⁺ sites. We further deduce that the low activity of RBVOM-A might result from the following reasons: (i) electron-hole recombination on single Rh³⁺ species, (ii) low OER activity of single Rh³⁺ sites undergoing single-site OER mechanism and (iii) poison of Rh–Cl coordination to bulk BVOM. It is mentionable that when pure BVOM was heat-treated either by air or hydrogen atmosphere, the photocatalytic OER performance also decreased (Figure S19), which demonstrates that it is isolated Rh⁰–Rh³⁺ sites instead of the heat treatment to bulk BVOM that activated the OER performance. Furthermore, the TOFs for RBVOM-H and RBVOM-A were calculated based on the dispersion of Rh³⁺ species on photocatalysts (see calculation details in the supporting information). In sharp contrast, the RBVOM-H gave a high TOF value of 416.73 h^{-1} , which is 378 times higher than RBVOM-A (1.10 h^{-1}). The great enhancement indicates the importance of generation of Rh⁰–Rh³⁺ sites.

Figure 3c shows the plotting of the UV-vis and apparent quantum yield (AQY) of the RBVOM-H as a function of wavelength of the incident light, and RBVOM-H presents an excellent AQY of 29.37% at 420 nm. Evaluating the photocatalytic oxygen production rate and AQY, an activity map of representative photocatalysts was constructed to intuitively showcase the photocatalytic OER performance of RBVOM-H. As shown in Figure 3d, RBVOM-H is in the best performance quadrant with impressive photocatalytic OER performance.^[2g,20] As the excellent performance of RBVOM-H, the photocatalytic sheet with the photocatalysts spraying on was prepared (Figure S20), showing the good film-forming property of the photocatalysts, which is necessary for water-splitting panels in advanced reactors for large scale applications.^[21] To further testify the photocatalytic performance of the sheet, a small size sheet was tested in the reactor (supplementary movie S1), exhibiting a photocatalytic oxygen production rate of $13.82 \text{ mmol m}^{-2} \text{ h}^{-1}$ (Figure S21).

Operando XAFS characterizations for photocatalytic OER

To gather the real structure-property relationship between the local Rh configuration and OER performance during the photocatalytic process, operando XAFS measurements for RBVOM-H and RBVOM-A were conducted. Figure 4a presents a schematic of the operando XAFS photocatalytic set-up which can help us observe the catalytic dynamic process. The Rh K-edge XANES spectra show the distinct differences between RBVOM-H and RBVOM-A (Figure 4b,c). In Figure 4b, the valence state of Rh in RBVOM-H increases gradually under the irradiation and dropped after turning off the irradiation, indicating the adsorption and desorption of oxygen-containing intermediates. For sharp comparison, the valence state of Rh in RBVOM-A keeps 3+ under the irradiation (Figure 4c), further demonstrating the important role of Rh^0 incorporation for oxygen generation. Figure 4d and 4e show the relationship between reaction time and Rh local coordination environment of RBVOM-H and RBVOM-A, respectively, with red regions between 1–2 Å represent Rh–O coordination. As shown in Figure 4d, the Rh–O coordination number increases with prolonged reaction time and would decrease after the reaction. This clearly evidences the reversible changes of Rh–O coordination configurations during the photocatalytic OER process. For comparison, the Rh–O coordination number almost remains unchanged during the reaction for RBVOM-A (Figure 4e), which is in line with the unchanged XANES spectra. Based on these results, we reason the $\text{Rh}^0\text{-Rh}^{3+}$ sites configurations instead of individual Rh^{3+} sites play an important role as the synergistic active sites for photocatalytic OER.

Theoretical exploration of the bifunctional $\text{Rh}^0\text{-Rh}^{3+}$ sites

The density functional theory (DFT) calculation was conducted systemically on Rh, Rh_2O_3 and $\text{Rh}^0/\text{Rh}_2\text{O}_3$ models (Figure 5a), which represent only Rh^0 sites, Rh^{3+} sites and

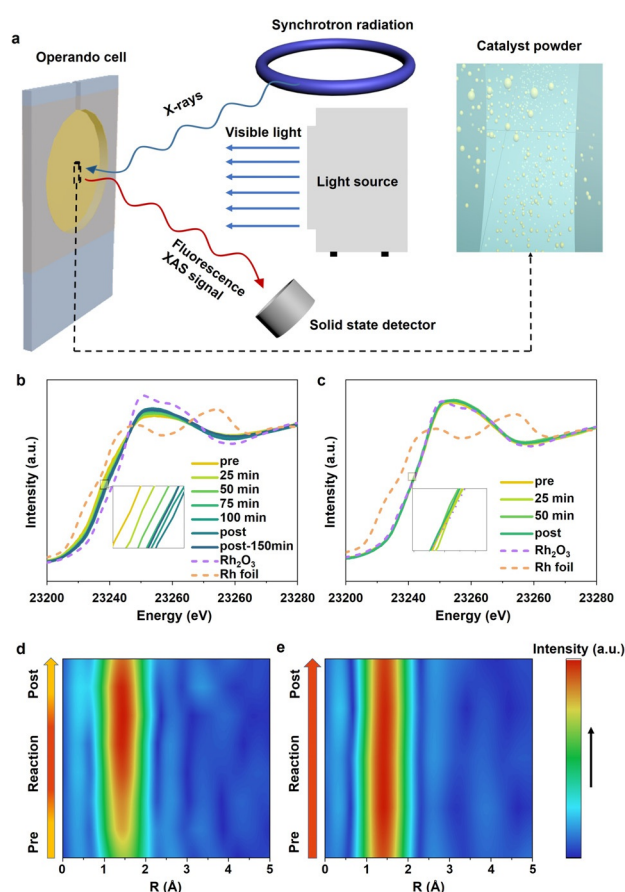


Figure 4. Operando XAFS to describe local structural evolution during photocatalytic OER process. a) Schematic illustration of the operando XAFS set-up, equipped with the operando cell with photocatalysts suspension in the solution. Operando Rh K-edge XANES spectra of b) RBVOM-H and c) RBVOM-A, indicating the valence states of Rh in RBVOM-H increased gradually but did not reach 3+ under irradiation, while the valence of Rh in RBVOM-A kept 3+. Corresponding time dependence of coordination environment for d) RBVOM-H and e) RBVOM-A, showing the reversible changes of Rh–O in RBVOM-H during the photocatalytic water oxidation process, which demonstrates the oxygen evolution process on the $\text{Rh}^0\text{-Rh}^{3+}$ cocatalyst instead of single Rh^{3+} sites. Notes: Pre represents the photocatalysts suspension in the solution without any irradiation; Reaction represents irradiation was carried out about 100 min for RBVOM-H and 50 min for RBVOM-A; Post represents the irradiation shutdown.

bifunctional $\text{Rh}^0\text{-Rh}^{3+}$ sites, respectively. The adsorption energies of H_2O on the individual Rh^0 and Rh^{3+} sites, as well as H intermediates on Rh^0 and lattice O near Rh^{3+} ($\text{Rh}^{3+}\text{-O}_{\text{lat}}$), were calculated, which proves the basic properties of different sites in adsorbing oxygen and transferred hydrogen intermediates. Comparing these adsorption energies (Figure S22), it is obvious that H_2O prefers to adsorb on the Rh^{3+} site with an adsorption energy of -0.96 eV rather than the Rh^0 site ($E_{\text{ads}} = -0.58 \text{ eV}$); while for H intermediates, contrarily it adsorbs on Rh^0 favorably instead of $\text{Rh}^{3+}\text{-O}_{\text{lat}}$ (-0.63 eV vs. -0.26 eV). Hence, it can be predicted that Rh^{3+} and Rh^0 could play important roles in oxygen and hydrogen intermediates adsorption, respectively, synergisti-

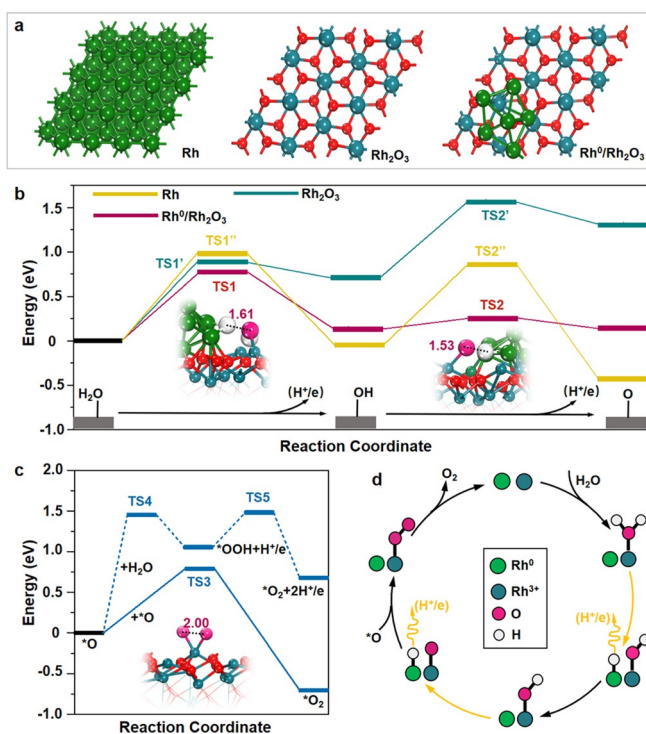


Figure 5. DFT calculations for the bifunctional Rh⁰-Rh³⁺ active sites. a) Rh, Rh₂O₃ and Rh⁰/Rh₂O₃ models used for DFT, which represents only Rh⁰, Rh³⁺ and bifunctional Rh⁰-Rh³⁺ sites, respectively. Rh₂O₃ was used to construct Rh³⁺ to simplify the system. b) The energy profile of H₂O dissociation on Rh, Rh₂O₃ and Rh⁰/Rh₂O₃ cocatalysts, showing the optimized energetics for OER on the bifunctional Rh⁰-Rh³⁺ sites. TS1 and TS2 are the transition state structures of H₂O and OH dehydrogenation at Rh⁰-Rh³⁺ active sites and other relative transition state structures are shown in Figure S23. c) The energy profiles of the O₂ formation by different pathways, indicating that the O-O coupling step is more feasible, and the relative transition states are shown in Figure S24. d) The proposed reaction mechanism for OER on the bifunctional Rh⁰-Rh³⁺ sites, showing the dehydrogenation process assisted by the Rh⁰ site promotes the adsorption of oxygen intermediates (*OH, *O and *OOH) on the Rh³⁺ site.

cally promoting the H₂O dissociation and subsequent dehydrogenation steps in the OER process.

To further demonstrate the promoting effect of the Rh⁰-Rh³⁺ sites on H₂O conversion, the related kinetic properties were also calculated (Figure 5b). On the Rh⁰-Rh³⁺ sites, the sequential dissociation of H₂O on Rh³⁺ into the atomic O species (*H₂O → *OH → *O, * represents Rh³⁺ site) with the H species released onto the metallic Rh⁰ sites simultaneously, exhibits relatively low energy barriers of 0.76 and 0.12 eV, respectively. These values are obviously lower than that on simple Rh⁰ sites (0.99 and 0.91 eV) or Rh³⁺ sites (0.89 and 0.85 eV). The structures of the optimized transition states are shown in Figure S23. Based on these thermodynamic and kinetic results, we anticipate that the Rh³⁺ site is in response to adsorb and activate H₂O, and the Rh⁰ site plays a key role to dehydrogenize H₂O and OH, facilitating O intermediates generation on the Rh³⁺ sites during the photocatalytic OER process. This is also consistent with operando XAFS results which shows the reversible changes in Rh-O coordination.

For the further oxygen generation steps on our catalysts, two common processes were considered:^[22] (i) *O + H₂O → *OOH + H⁺/e⁻, *OOH → O₂ + * + H⁺/e⁻; and (ii) *O + *O → O₂ + * + * (* represents Rh³⁺ site). The pathway (i), i.e., H₂O attacking the adsorbed O to form the O-O bond, can be also accelerated by hydrogen anchoring onto the metallic Rh⁰ site with an energy barrier of 1.45 eV (vs. 3.42 eV on Rh⁰ and 1.65 eV on Rh³⁺). In comparison, the pathway (ii), i.e., the O-O coupling step on Rh³⁺ site is easier to occur, which has a lower energy barrier of 0.78 eV (Figure 5c). Therefore, we believe the OER energetics of both steps can be optimized via Rh⁰ site incorporation for dehydrogenation, and propose an energetically favoured OER mechanism that might occur as follows (Figure 5d): H₂O prefers to adsorb on the Rh³⁺ site and dissociates into O atom assisted by the Rh⁰ site, then the formed O atoms on the Rh³⁺ sites can couple each other to form O-O bond, finishing the whole water oxidation cycle.

Overall, the Rh³⁺ and Rh⁰ sites at the Rh⁰-Rh³⁺ sites configuration cooperate to complete the whole catalytic process, and the promoting effect can be ascribed to that the Rh³⁺ sites afford the efficient binding sites for O intermediates (*OH, *O and *OOH) and the Rh⁰ sites contribute to the adsorption of H species. Such a bifunctional mechanism can make full use of the adsorption selectivity of different-valent-state species to different adsorbates, thus breaking the scaling relationship to improve the whole catalytic activity.

Conclusion

In this work, we construct an isolated Rh_n OER cocatalyst with Rh⁰-Rh³⁺ sites anchored on Mo-doped BiVO₄, which delivers a super high visible-light photocatalytic oxygen production activity of 7.11 mmol g⁻¹ h⁻¹ and an AQY of 29.37% at 420 nm. Compared to RBVOM-A, the TOF of RBVOM-H improves 378 times. The XPS, XAFS as well as theoretical simulations confirm the coexistence of Rh⁰ and Rh³⁺ sites in the isolated Rh_n cocatalyst. The operando XAFS results show the distinct reversible Rh-O configurations during the OER process on RBVOM-H, which unambiguously demonstrate the bifunctional Rh⁰-Rh³⁺ sites instead of Rh³⁺ single sites as OER active sites. The DFT calculations further illustrate the bifunctional OER mechanism on the Rh⁰-Rh³⁺ sites, with the oxygen intermediate attacks the Rh³⁺ sites facilitated by a hydrogen atom transfers to the adjacent Rh⁰ sites, which synergistically optimize OER energetics. This cocatalyst consisting of synergistic sites with different-valent-state atoms would open up a new avenue to potentially break OER scaling relationships, which can be further used in the OER-related solar-to-hydrogen conversion techniques.

Acknowledgements

This work was financially supported by the National Natural Science Funds for Distinguished Young Scholars (51725201), the International (Regional) Cooperation and Exchange Projects of the National Natural Science Foundation of China

(51920105003), the Innovation Program of Shanghai Municipal Education Commission (E00014), the National Natural Science Foundation of China (51902105, 21902048), the Shanghai Engineering Research Center of Hierarchical Nanomaterials (18DZ2252400) and the Shanghai Sailing Program (19YF1411600). The authors also thank the Frontiers Science Center for Materiobiology and Dynamic Chemistry. The authors also thank the crew of the BL14W1 beamline at the Shanghai Synchrotron Radiation Facility (SSRF) and the 1W1B beamline of Beijing Synchrotron Radiation Facility (BSRF) for their constructive assistance with the XAFS measurements and data analyses.

Conflict of Interest

The authors declare no conflict of interest.

Keywords: cocatalyst · oxygen evolution reaction · photocatalysts · rhodium

- [1] a) X. Chen, S. Shen, L. Guo, S. S. Mao, *Chem. Rev.* **2010**, *110*, 6503–6570; b) S. J. Davis, N. S. Lewis, M. Shaner, S. Aggarwal, D. Arent, I. L. Azevedo, S. M. Benson, T. Bradley, J. Brouwer, Y.-M. Chiang, C. T. M. Clack, A. Cohen, S. Doig, J. Edmonds, P. Fennell, C. B. Field, B. Hannegan, B.-M. Hodge, M. I. Hoffert, E. Ingersoll, P. Jaramillo, K. S. Lackner, K. J. Mach, M. Mastrandrea, J. Ogden, P. F. Peterson, D. L. Sanchez, D. Sperling, J. Stagner, J. E. Trancik, C.-J. Yang, K. Caldeira, *Science* **2018**, *360*, eaas9793; c) N. S. Lewis, *Science* **2016**, *351*, aad1920.
- [2] a) R. Asahi, T. Morikawa, T. Ohwaki, K. Aoki, Y. Taga, *Science* **2001**, *293*, 269–271; b) A. Kongkanand, K. Tvrđy, K. Takechi, M. Kuno, P. V. Kamat, *J. Am. Chem. Soc.* **2008**, *130*, 4007–4015; c) E. Borgarello, J. Kiwi, E. Pelizzetti, M. Visca, M. Grätzel, *Nature* **1981**, *289*, 158–160; d) A. Primo, T. Marino, A. Corma, R. Molinari, H. García, *J. Am. Chem. Soc.* **2011**, *133*, 6930–6933; e) X. Chen, L. Liu, P. Y. Yu, S. S. Mao, *Science* **2011**, *331*, 746–750; f) X. Wang, K. Maeda, A. Thomas, K. Takanebe, G. Xin, J. M. Carlsson, K. Domen, M. Antonietti, *Nat. Mater.* **2009**, *8*, 76–80; g) Z. Yi, J. Ye, N. Kikugawa, T. Kako, S. Ouyang, H. Stuart-Williams, H. Yang, J. Cao, W. Luo, Z. Li, Y. Liu, R. L. Withers, *Nat. Mater.* **2010**, *9*, 559–564; h) D. J. Martin, N. Umezawa, X. Chen, J. Ye, J. Tang, *Energy Environ. Sci.* **2013**, *6*, 3380–3386.
- [3] a) J. Ran, J. Zhang, J. Yu, M. Jaroniec, S. Z. Qiao, *Chem. Soc. Rev.* **2014**, *43*, 7787–7812; b) J. Yang, D. Wang, H. Han, C. Li, *Acc. Chem. Res.* **2013**, *46*, 1900–1909.
- [4] a) B. Kraeutler, A. J. Bard, *J. Am. Chem. Soc.* **1978**, *100*, 5985–5992; b) B. Kraeutler, A. J. Bard, *J. Am. Chem. Soc.* **1978**, *100*, 4317–4318.
- [5] a) J. Ran, G. Gao, F. T. Li, T. Y. Ma, A. Du, S. Z. Qiao, *Nat. Commun.* **2017**, *8*, 13907; b) J. Ran, B. Zhu, S. Z. Qiao, *Angew. Chem. Int. Ed.* **2017**, *56*, 10373–10377; *Angew. Chem.* **2017**, *129*, 10509–10513; c) K. Sun, M. Liu, J. Pei, D. Li, C. Ding, K. Wu, H.-L. Jiang, *Angew. Chem. Int. Ed.* **2020**, *59*, 22749–22755; *Angew. Chem.* **2020**, *132*, 22937–22943.
- [6] a) J. Xing, H. B. Jiang, J. F. Chen, Y. H. Li, L. Wu, S. Yang, L. R. Zheng, H. F. Wang, P. Hu, H. J. Zhao, H. G. Yang, *J. Mater. Chem. A* **2013**, *1*, 15258–15264; b) Y. H. Li, J. Xing, Z. J. Chen, Z. Li, F. Tian, L. R. Zheng, H. F. Wang, P. Hu, H. J. Zhao, H. G. Yang, *Nat. Commun.* **2013**, *4*, 2500; c) J. Liu, Y. Li, X. Zhou, H. Jiang, H. G. Yang, C. Li, *J. Mater. Chem. A* **2020**, *8*, 17–26.
- [7] N.-T. Suen, S.-F. Hung, Q. Quan, N. Zhang, Y.-J. Xu, H. M. Chen, *Chem. Soc. Rev.* **2017**, *46*, 337–365.
- [8] a) M. T. M. Koper, *J. Electroanal. Chem.* **2011**, *660*, 254–260; b) H. B. Tao, J. Zhang, J. Chen, L. Zhang, Y. Xu, J. G. Chen, B. Liu, *J. Am. Chem. Soc.* **2019**, *141*, 13803–13811.
- [9] a) Y. Chen, S. Ji, W. Sun, Y. Lei, Q. Wang, A. Li, W. Chen, G. Zhou, Z. Zhang, Y. Wang, L. Zheng, Q. Zhang, L. Gu, X. Han, D. Wang, Y. Li, *Angew. Chem. Int. Ed.* **2020**, *59*, 1295–1301; *Angew. Chem.* **2020**, *132*, 1311–1317; b) B.-H. Lee, S. Park, M. Kim, A. K. Sinha, S. C. Lee, E. Jung, W. J. Chang, K.-S. Lee, J. H. Kim, S.-P. Cho, H. Kim, K. T. Nam, T. Hyeon, *Nat. Mater.* **2019**, *18*, 620–626.
- [10] a) J. M. P. Martínez, E. A. Carter, *J. Am. Chem. Soc.* **2019**, *141*, 693–705; b) M. Busch, N. B. Halck, U. I. Kramm, S. Siahrostami, P. Krtil, J. Rossmeisl, *Nano Energy* **2016**, *29*, 126–135; c) L. Bai, S. Lee, X. Hu, *Angew. Chem. Int. Ed.* **2021**, *60*, 3095–3103; *Angew. Chem.* **2021**, *133*, 3132–3140.
- [11] a) R. Li, F. Zhang, D. Wang, J. Yang, M. Li, J. Zhu, X. Zhou, H. Han, C. Li, *Nat. Commun.* **2013**, *4*, 1432; b) Q. Wang, T. Hisatomi, Q. Jia, H. Tokudome, M. Zhong, C. Wang, Z. Pan, T. Takata, M. Nakabayashi, N. Shibata, Y. Li, I. D. Sharp, A. Kudo, T. Yamada, K. Domen, *Nat. Mater.* **2016**, *15*, 611–615; c) Q. Wang, J. Warnan, S. Rodríguez-Jiménez, J. J. Leung, S. Kalathil, V. Andrei, K. Domen, E. Reisinger, *Nat. Energy* **2020**, *5*, 703–710; d) L. Pan, J. H. Kim, M. T. Mayer, M.-K. Son, A. Ummadisingu, J. S. Lee, A. Hagfeldt, J. Luo, M. Grätzel, *Nat. Catal.* **2018**, *1*, 412–420; e) B. Zhang, L. Wang, Y. Zhang, Y. Ding, Y. Bi, *Angew. Chem. Int. Ed.* **2018**, *57*, 2248–2252; *Angew. Chem.* **2018**, *130*, 2270–2274; f) Q. Hu, X. Meng, Y. Dong, Q. Han, Y. Wang, Y. Ding, *Chem. Commun.* **2019**, *55*, 11778–11781; g) X. Liang, J. Lin, X. Cao, W. Sun, J. Yang, B. Ma, Y. Ding, *Chem. Commun.* **2019**, *55*, 2529–2532; h) S. Ye, C. Ding, R. Chen, F. Fan, P. Fu, H. Yin, X. Wang, Z. Wang, P. Du, C. Li, *J. Am. Chem. Soc.* **2018**, *140*, 3250–3256.
- [12] A. Kudo, K. Omori, H. Kato, *J. Am. Chem. Soc.* **1999**, *121*, 11459–11467.
- [13] A. Wong, Q. Liu, S. Griffin, A. Nicholls, J. R. Regalbutto, *Science* **2017**, *358*, 1427–1430.
- [14] R. Li, H. Han, F. Zhang, D. Wang, C. Li, *Energy Environ. Sci.* **2014**, *7*, 1369–1376.
- [15] X. Lin, D. Xu, Y. Xi, R. Zhao, L. Zhao, M. Song, H. Zhai, G. Che, L. Chang, *Colloids Surf. A* **2017**, *513*, 117–124.
- [16] a) A. Talo, J. Lahtinen, P. Hautiojärvi, *Appl. Catal. B* **1995**, *5*, 221–231; b) L. Wang, W. Zhang, S. Wang, Z. Gao, Z. Luo, X. Wang, R. Zeng, A. Li, H. Li, M. Wang, X. Zheng, J. Zhu, W. Zhang, C. Ma, R. Si, J. Zeng, *Nat. Commun.* **2016**, *7*, 14036.
- [17] L. Han, D. Mao, J. Yu, Q. Guo, G. Lu, *Catal. Commun.* **2012**, *23*, 20–24.
- [18] O. Bunäu, Y. Joly, *J. Phys. Condens. Matter* **2009**, *21*, 345501.
- [19] Z. Xia, H. Zhang, K. Shen, Y. Qu, Z. Jiang, *Phys. B* **2018**, *542*, 12–19.
- [20] a) S. S. K. Ma, T. Hisatomi, K. Maeda, Y. Moriya, K. Domen, *J. Am. Chem. Soc.* **2012**, *134*, 19993–19996; b) F. Zhang, A. Yamakata, K. Maeda, Y. Moriya, T. Takata, J. Kubota, K. Teshima, S. Oishi, K. Domen, *J. Am. Chem. Soc.* **2012**, *134*, 8348–8351; c) X. Tao, Y. Gao, S. Wang, X. Wang, Y. Liu, Y. Zhao, F. Fan, M. Dupuis, R. Li, C. Li, *Adv. Energy Mater.* **2019**, *9*, 1803951; d) H. G. Kim, D. W. Hwang, J. S. Lee, *J. Am. Chem. Soc.* **2004**, *126*, 8912–8913; e) P. Li, X. Chen, H. He, X. Zhou, Y. Zhou, Z. Zou, *Adv. Mater.* **2018**, *30*, 1703119; f) C. Dong, S. Lu, S. Yao, R. Ge, Z. Wang, Z. Wang, P. An, Y. Liu, B. Yang, H. Zhang, *ACS Catal.* **2018**, *8*, 8649–8658; g) H. L. Tan, X. Wen, R. Amal, Y. H. Ng, *J. Phys. Chem. Lett.* **2016**, *7*, 1400–1405; h) T. Wei, Y. Zhu, Z. Gu, X. An, L.-m. Liu, Y. Wu, H. Liu, J. Tang, J. Qu, *Nano Energy* **2018**, *51*, 764–773; i) S. Chen, S. Shen, G. Liu, Y. Qi, F. Zhang, C. Li, *Angew. Chem. Int. Ed.* **2015**, *54*, 3047–3051; *Angew. Chem.* **2015**, *127*, 3090–3094; j) C. G. Silva, Y. Bouizvi, V. Fornés, H. García, *J. Am. Chem. Soc.* **2009**, *131*, 13833–13839; k) Y. Zhao, B. Li, Q. Wang, W. Gao, C. J. Wang,

- M. Wei, D. G. Evans, X. Duan, D. O'Hare, *Chem. Sci.* **2014**, *5*, 951–958.
- [21] T. Hisatomi, K. Domen, *Nat. Catal.* **2019**, *2*, 387–399.
- [22] a) Y. Zhou, S. Sun, C. Wei, Y. Sun, P. Xi, Z. Feng, Z. J. Xu, *Adv. Mater.* **2019**, *31*, 1902509; b) D. Wang, T. Sheng, J. Chen, H.-F. Wang, P. Hu, *Nat. Catal.* **2018**, *1*, 291–299.

Manuscript received: May 22, 2021
Accepted manuscript online: June 25, 2021
Version of record online: July 19, 2021
